ELSEVIER

Polymer 42 (2001) 699–712

polymer

www.elsevier.nl/locate/polymer

Isothermal melt- and cold-crystallization kinetics and subsequent melting behavior in syndiotactic polypropylene: a differential scanning calorimetry study

P. Supaphol[a,*], J.E. Spruiell[b]

[a]*The Petroleum and Petrochemical College, Chulalongkorn University, Bangkok 10330, Thailand*
[b]*Materials Science and Engineering, University of Tennessee, Knoxville, TN 37996, USA*

Received 22 December 1999; received in revised form 14 April 2000; accepted 12 May 2000

Abstract

The isothermal melt- and cold-crystallization kinetics and subsequent melting behavior of syndiotactic polypropylene (*s*-PP) were investigated using differential scanning calorimetry (DSC). The overall crystallization kinetics was determined by directly fitting the experimental data to the Avrami and Malkin macrokinetic models using a non-linear multi-variable regression program. When plotted as a function of crystallization temperature, the overall crystallization rate parameters for melt-crystallization process exhibited an unmistakable double bell-shaped curve, while those for cold-crystallization process showed the typical bell-shaped curve. Comparison of the overall crystallization rate parameters obtained for both melt- and cold-crystallization processes indicated that crystallization from the glassy state proceeded at a much greater rate than that from the melt state. Melting of samples isothermally crystallized at low and moderate crystallization temperatures exhibited multiple-melting phenomenon. Determination of the equilibrium melting temperature according to the "linear" and "non-linear" Hoffman–Weeks extrapolative methods provided values of ca. 145 and 182°C, respectively.

Keywords: Melt-crystallization kinetics; Cold-crystallization kinetics; Multiple-melting behavior

1. Introduction

The syndiotactic form of polypropylene (*s*-PP) has largely been a laboratory curiosity since it was first produced in the 1960s by Natta et al. [1,2]. It has gained more interest in terms of industrial applications since 1988 when Ewen et al. [3] reported that highly stereo-regular and regio-regular *s*-PP can be synthesized using novel metallocene catalysis. Since then, industrial applications of *s*-PP have been extensively explored in areas such as films [4,5], injection molding [6] and melt-spun fibers [7,8]. Other physical properties related to applications have also been investigated and reported [9,10].

Studies related to the crystallization process of semicrystalline polymers are of great importance in polymer processing, owing to the fact that the resulting physical properties are strongly dependent on the morphology formed and the extent of crystallization. It is therefore very important to understand the processing-structure–property inter-relationships of the studied materials, which in this case is *s*-PP. Investigations related to the chain conformation, crystal structure, morphology and phase transitions in *s*-PP have been reported extensively in recent years. These studies up to 1994 were reviewed and discussed in a publication by Rodriguez-Arnold et al. [11]. Studies which have been carried out in the subject of isothermal crystallization of *s*-PP include the Avrami kinetics of the crystallization process [12–14], the kinetics of the linear growth rates [13,15,16] and the morphology of the single crystals [17].

In this manuscript, the overall kinetics of crystallization under isothermal quiescent conditions from both the melt and glassy states (i.e. melt- and cold-crystallization processes) and subsequent melting behavior of *s*-PP is thoroughly investigated using differential scanning calorimetry (DSC).

2. Theoretical background

Overall crystallization of semi-crystalline polymers involves two main processes: primary and secondary crystallization. Primary crystallization relates to macroscopic

* Corresponding author. Tel.: +66-2-218-4134; fax: +66-2-215-4459.
E-mail address: ps@sunsv1.ppc.chula.ac.th (P. Supaphol).

0032-3861/01/$ - see front matter
PII: S0032-3861(00)00399-2

development of crystallinity as a result of two consecutive microscopic mechanisms: primary and secondary nucleation (i.e. subsequent crystal growth). Formation of chain-folded lamellae leads to further growth of the lamellae through the processes of branching and splaying (see Ref. [18, Fig. 4]). The magnitude of branching and splaying is mainly controlled by the degree of undercooling (i.e. the difference between the equilibrium melting temperature T_m^0 and the crystallization temperature T_c : $\Delta T = T_m^0 - T_c$). In general, the magnitude of branching and splaying increase with increasing degree of undercooling. An evidence to this assertion can be seen in a series of atomic force microscopy (AFM) images of the crystal growth in *i*-PS taken by Taguchi et al. [19], in which they showed that the magnitude of branching and splaying in crystalline aggregates increases with increasing degree of undercooling. This leads to the change of the crystalline aggregates from being a hexagon platelet at $T_c = 210$°C to being a dense-branched morphology (spherulitic in 2D) at $T_c = 180$°C. The primary crystallization is assumed to cease when no additional molecular stems can transport onto a growth face. This may be due to the impingement of the crystalline aggregates onto one another.

Secondary crystallization refers to any process that leads to further increase in crystallinity (after the cessation of the primary crystallization process). Two important processes are envisaged: (1) crystal perfection and/or thickening of the primary lamellae; and (2) formation of secondary lamellae from crystallizable melt trapped between two different lamellae in the same stack (i.e. inter-lamellar crystallizable melt) or between two different stacks of lamellae (i.e. inter-fibrillar crystallizable melt). The thickening mechanism is thermodynamically driven by the reduction of the specific surfaces of the crystals (hence less free energy penalty for the formation of surfaces), but is hampered by the kinetics factors (e.g. molecular mobility). Even though it is obvious that secondary lamellae have to somehow originate from either inter-lamellar or inter-fibrillar crystallizable melt (or both) trapped within the crystalline aggregates (e.g. axialites, spherulites, etc.) [20–22] after their impingement, the mechanisms by which the formation of the secondary lamellae are formed are uncertain and are still matters of ongoing research (e.g. Ref. [23]).

In order to describe the macroscopic evolution of crystallinity under isothermal quiescent conditions (during the primary crystallization process), a number of mathematical models [24–33] have been proposed over the past 60 years. Even though contributions from Kolmogoroff [24], Johnson and Mehl [25], Avrami [26–28] and Evans [29] are essentially similar in their final results, it is the work of Avrami that has received the most attention and as a result these contributions are frequently referred to as the "Avrami" macrokinetic model. In addition to the Avrami model, there is the Tobin macrokinetic model [30–32] which was essentially a modification to the Avrami model in order to account for the impingement of crystalline aggregates, and Malkin macrokinetic model [33] which was derived based totally on a different theoretical approach from the other two models. Recently, we used a non-linear multi-variable regression program to fit the isothermal crystallization measurements from DSC to all of the models mentioned above [34]. Only the Avrami and Malkin models were found to be satisfactory in describing the experimental data and this is the reason for our use of only these two macrokinetic models in describing our experimental data in the present manuscript.

If $\chi_{c,\infty}$ and $\chi_c(t)$ are the ultimate crystallinity obtained after complete crystallization at a given crystallization temperature T_c and the instantaneous crystallinity after partial crystallization for a given crystallization time t at the same crystallization temperature T_c, respectively, then the Avrami equation [24–29] governing the phase transformation during primary crystallization is given by

$$\frac{\chi_c(t)}{\chi_{c,\infty}} = \theta(t) = 1 - \exp(-k_a t^{n_a}) \in [0,1], \tag{1}$$

where $\theta(t)$ is the relative crystallinity as a function of time, k_a is the Avrami crystallization rate constant and n_a is the Avrami exponent of time. Both k_a and n_a are constants typical of a given crystalline morphology and type of nucleation for a particular crystallization condition [35]. It should be noted that, according to the original assumptions of the theory, the value of n_a should be integral, ranging from 1 to 4.

Derived based on the notion that the overall crystallization rate equals the summation of the rate at which the degree of crystallinity varies as a result of the emergence of the primary nuclei and the rate of variation in the degree of crystallinity as a result of crystal growth, Malkin et al. [33] proposed a totally different mocrokinetic model as follows:

$$\frac{\chi_c(t)}{\chi_{c,\infty}} = \theta(t) = 1 - \frac{C_0 + 1}{C_0 + \exp(C_1 t)} \in [0,1] \tag{2}$$

where $\theta(t)$ denotes the relative crystallinity as a function of time. C_0 relates directly to the ratio of the secondary nucleation rate or the linear crystal growth rate G to the primary nucleation rate I (i.e. $C_0 \propto G/I$) and C_1 relates directly to the overall crystallization rate (i.e. $C_1 = a \cdot I + b \cdot G$, where a and b are specific constants). Apparently, both C_0 and C_1 are temperature-dependent constants.

Analysis of the experimental data based on the Avrami approach is straightforward. Traditionally, the Avrami kinetics parameters, k_a and n_a, can be extracted from a least-square line fitted to the double logarithmic plot of $\ln[-\ln(1 - \theta(t))]$ versus $\ln(t)$; k_a is the anti-logarithmic value of the y-intercept and n_a is the slope of the least-square line. On the contrary, the Malkin kinetics parameters, C_0 and C_1, cannot be obtained as easily; therefore, Malkin et al. [33] suggested a way to estimate their kinetics parameters, C_0 and C_1, based on the information obtained from the Avrami

analysis. Hence, the Malkin exponent and rate parameters can be written as

$$C_0 = 4^{n_a} - 4, \tag{3}$$

and

$$C_1 = \ln(4^{n_a} - 2)\left(\frac{k_a}{\ln(2)}\right)^{1/n_a}. \tag{4}$$

Instead of analyzing the experimental data using the traditional procedure mentioned in the previous paragraph, we use a non-linear multi-variable regression program to directly fit the experimental data to the Avrami and Malkin macrokinetic models [34]. The corresponding kinetics parameters indicated in each model are automatically provided by the program along with the best fit.

3. Experimental details

3.1. Materials

The *s*-PP resin (labeled in this present manuscript as *s*-PP#1) used in this study was synthesized using metallocene catalysis and was produced commercially in pellet form by Fina Oil and Chemical Company of La Porte, TX. Molecular characterization data shows the following molecular weight information: $M_n = 76,200$ Da, $M_w = 165,000$ Da, $M_z = 290,000$ Da and $M_w/M_n = 2.2$. In addition, the syndiotacticity measured by ^{13}C NMR shows the racemic dyad content [%*r*] to be 91.4%, the racemic triad content [%*rr*] to be 87.3% and the racemic pentad content [%*rrrr*] to be 77.1%. The glass transition temperature T_g was determined to be ca. -6°C [14].

3.2. Sample preparation and technique

Sliced pellets were melt-pressed under a pressure of ca. 4.6×10^2 MN m^{-2} between a pair of polyimide films, which in turn were sandwiched between a pair of thick metal plates, in a Wabash compression molding machine preset at 190°C. After 10 min holding time, a film of ca. 280 μm thickness was taken out and allowed to cool at ambient condition down to room temperature between the two metal plates. This treatment assumes that previous thermo-mechanical history was essentially erased, and provides a standard crystalline memory condition for our experiments.

In this study, a differential scanning calorimeter (DSC-7, Perkin–Elmer) was used to follow isothermal crystallization behavior of *s*-PP. The DSC-7 equipped with internal liquid nitrogen cooling unit reliably provided a cooling rate up to 200°C min^{-1}. Temperature calibration was performed using an indium standard ($T_m^0 = 156.6$°C and $\Delta H_f^0 = 28.5$ J g^{-1}). The consistency of the temperature calibration was checked every other run to ensure reliability of the data obtained. To make certain that thermal lag between the polymer sample and the DSC sensors is kept to a minimum, each sample holder was loaded with a single disc, weighed around 4.9 ± 0.3 mg, which was cut from the as-prepared film. It is noteworthy that each sample was used only once and all the runs were carried out under nitrogen atmosphere.

3.3. Methods

For isothermal crystallization from the melt state, each sample was melted in a Mettler hot-stage at a fusion temperature T_f of 190°C for 5 min to ensure complete melting [36]. The sample was then transferred as quickly as possible to the DSC cell, the temperature of which was preset at a desired crystallization temperature T_c ranging from 10 to 95°C. Immediately after complete crystallization at T_c, the sample was heated without prior cooling at a constant scanning rate of 20°C min^{-1} to observe its melting behavior. In order to investigate whether or not premature crystallization occurs during sample transfer and thermal stabilization (between sample and the DSC furnace), we performed separate experiments in which, instead of waiting for each sample to completely crystallize at the designated crystallization temperature T_c, heating scan was immediately performed on the sample as soon as thermal stabilization was reached. According to these experiments, melting peaks, which are negligibly small, were only observed in subsequent heating scans of samples which we attempted to study at the lowest crystallization temperatures (i.e. $T_c = 10$ and 12.5°C). These findings ascertain that premature crystallization for the majority of the conditions studied (i.e. $15 \le T_c \le 95$°C) did not occur, and the data obtained are for strictly isothermal condition from the melt state.

For isothermal crystallization from the glassy state, each sample was melted in a Mettler hot-stage at a fusion temperature T_f of 190°C for 5 min to ensure complete melting [36], before being quenched in liquid nitrogen. After submergence in liquid nitrogen for 3 min, each sample was transferred as quickly as possible to the DSC cell, the temperature of which was preset at a desired crystallization temperature T_c ranging from 8 to 100°C. Immediately after complete crystallization at T_c, the sample was heated without prior cooling at a constant scanning rate of 20°C min^{-1} to observe its melting behavior. In order to investigate whether or not premature crystallization occurs during sample transfer and thermal stabilization, similar separate experiments as described in the previous paragraph were performed. According to these experiments, melting peaks, which are negligibly small, were only observed in subsequent heating scans of samples crystallized at the highest crystallization temperatures studied (i.e. $T_c = 92.5$ and 100°C). These findings indicate that premature crystallization for the majority of the conditions studied (i.e. $8 \le T_c \le 87.5$°C) did not occur, and the data obtained represent strictly isothermal crystallization from the glassy state.

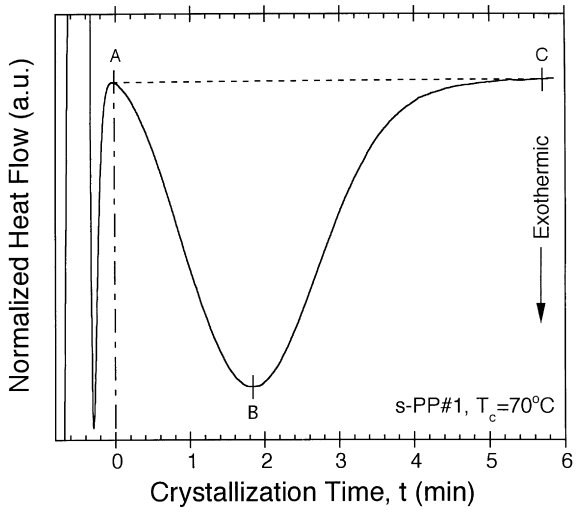

Fig. 1. Typical crystallization exotherm data of *s*-PP sample isothermally crystallized at $T_c = 70°C$ from the melt state.

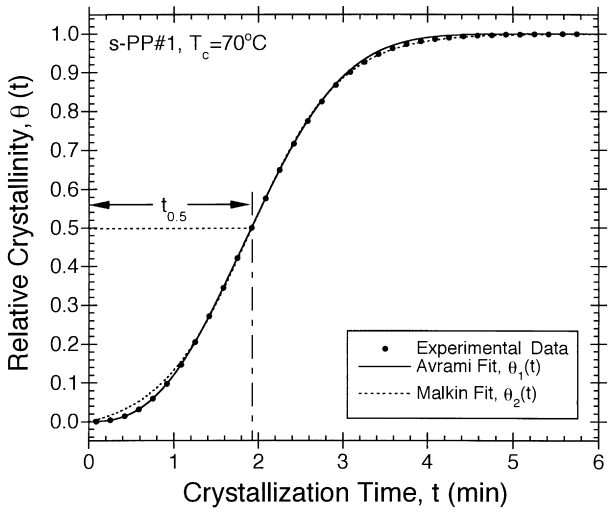

Fig. 2. Typical relative crystallinity $\theta(t)$ as a function of crystallization time t, calculated from the raw crystallization exotherm data shown in Fig. 1 according to Eq. (6).

4. Results

4.1. Crystallization kinetics

Fig. 1 shows a typical DSC crystallization exotherm for isothermal crystallization from the melt state of *s*-PP#1 at $T_c = 70°C$ after complete melting at 190°C for 5 min. Crystallization is assumed to begin at point A, which is preceded by a short period in which the temperature of the sample is equilibrated to T_c. Increasing heat flow due to evolution of the enthalpy of crystallization is evident until a maximum is observed at point B. The rate of evolution of the enthalpy of crystallization depends strongly on the kinetics of the crystallization process, which is very sensitive to changes in crystallization temperature T_c. After point B, crystallization slows down significantly, and the measurement is terminated (i.e. at point C) when no noticeable change in the heat flow is further detected.

Intuitively, during crystallization of semi-crystalline polymers under isothermal conditions, it is assumed that the observed heat flow is directly proportional to the weight of the sample w, the enthalpy of crystallization ΔH_c and the instantaneous crystallization rate $\dot{\theta}(t)$. The enthalpy of crystallization is the product of the final degree of crystallinity $\chi_{c,\infty}$ and the enthalpy of crystallization of an infinitely thick crystal ΔH_c^0 (i.e. 100% crystalline sample). Consequently, we may write an equation for the heat flow as

$$Q = c_1 \cdot w \cdot \chi_{c,\infty} \cdot \Delta H_c^0 \cdot \dot{\theta}(t), \tag{5}$$

where c_1 is a combined physical constant specific for each DSC used.

By setting $\dot{q} = \dot{Q}/(c_1 \cdot w \cdot \chi_{c,\infty} \cdot \Delta H_c^0)$, the relative crystallinity $\theta(t)$ can be obtained by an integration of the transient normalized heat flow $\dot{q}(t)$ over the course of the crystallization. One finally gets

$$\theta(t) = \int_0^t \dot{\theta}(t')\,dt' = \int_0^t \dot{q}(t')\,dt'. \tag{6}$$

Fig. 2 shows a plot of relative crystallization $\theta(t)$ as a function of crystallization time t, which was calculated from the heat flow data shown in Fig. 1 according to Eq. (2). An important parameter, which can be readily measured from the relative crystallinity plot similar to Fig. 2, is the half-time of crystallization $t_{0.5}$, which is defined as the time spent from the onset of the crystallization to the point where the crystallization is 50% complete. It should be noted that the reciprocal value of the crystallization half-time (i.e. $t_{0.5}^{-1}$) is often used to characterize the overall rate of the crystallization process.

In order to obtain kinetics information specific for the Avrami and Malkin models, the experimental relative crystallization data $\theta(t)$ such as that shown in Fig. 2 are directly fitted to each respective model using a non-linear multivariable regression program. It is demonstrated in Fig. 2 for the case of isothermal crystallization at $T_c = 70°C$ that the experimental data shown can be described by an Avrami equation of the form (shown in Fig. 2 as the solid line $\theta_1(t)$):

$$\theta(t) = 1 - \exp(-1.29 \times 10^{-1} \cdot t^{2.58}), \tag{7}$$

or it can be described by a Malkin equation of the form (shown in Fig. 2 as the dotted line $\theta_2(t)$):

$$\theta(t) = 1 - \frac{37.3}{36.3 + \exp(1.90 \cdot t)}; \tag{8}$$

which gives us the values of the corresponding kinetics parameters as the following: the Avrami exponent $n_a = 2.58$, the Avrami rate constant $k_a = 1.29 \times 10^{-1}\ \text{min}^{-2.58}$, the Malkin exponent $C_0 = 36.3$ and finally the Malkin rate constant $C_1 = 1.90\ \text{min}^{-1}$. It should be noted that only the

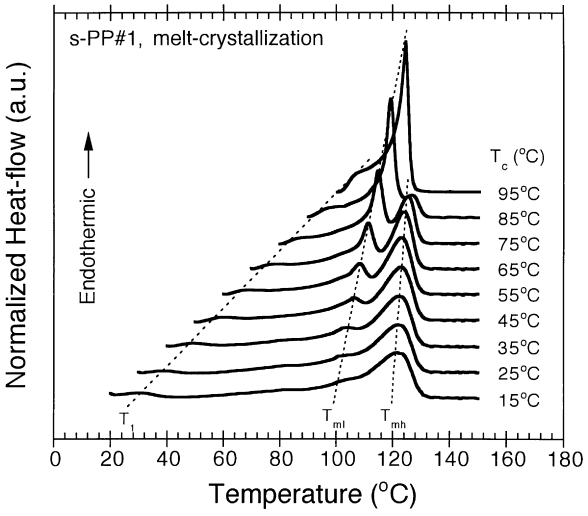

Fig. 3. Subsequent melting endotherms (20°C min^{-1}) of *s*-PP samples after isothermal crystallization from the melt state at the specified temperatures. Terminologies: T_1, the minor peak temperature; T_{ml}, the low-melting peak temperature and T_{mh}, the high-melting peak temperature.

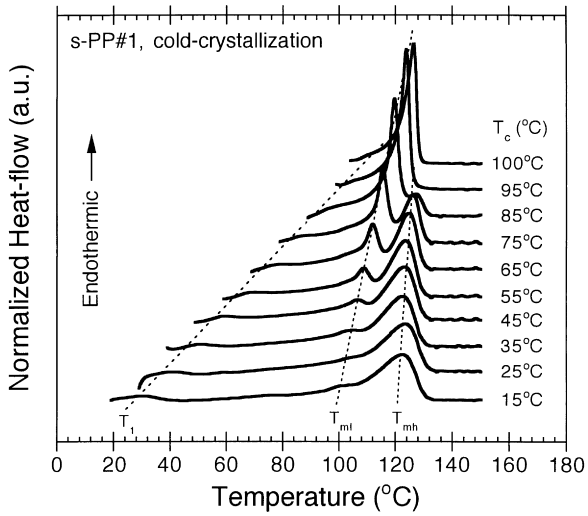

Fig. 4. Subsequent melting endotherms (20°C min^{-1}) of *s*-PP samples after isothermal crystallization from the glassy state at the specified temperatures. Terminologies: T_1, the minor peak temperature; T_{ml}, the low-melting peak temperature and T_{mh}, the high-melting peak temperature.

data in the range of $\theta(t) \in [0.10,0.80]$ were used in the analysis.

By repeating the analytical procedure described above on all of the experimental data collected over a wide range of crystallization temperatures T_c (from 10 to 95°C for crystallization from the melt state and from 8 to 100°C for crystallization from the glassy state with 2.5°C increment between each data point), related kinetics parameters (i.e. $t_{0.5}^{-1}$, n_a, k_a, C_0 and C_1) for describing isothermal crystallization process of *s*-PP#1 at various crystallization temperatures can be obtained. Since the temperature dependence of the experimental data is graphically presented and discussed in detail in the discussion section, inclusion of the quantitative summary of these data (in the form of tables) in this manuscript was not warranted (by the reviewing board) for fear that the summary might appear to be a duplication of the graphical presentations of the data. Interested readers, however, are welcome to request for this summary from the corresponding author.

4.2. Subsequent melting behavior

Figs. 3 and 4 illustrate two sets of DSC melting endotherms (20°C min^{-1}) which were recorded after complete crystallization from the melt and glassy states at different crystallization temperatures, respectively. Referring to all of the subsequent DSC melting endotherms recorded, it is evident that either two or three melting endotherms are observed. Whether two or three melting endotherms are observed depends greatly on the temperature range at which the samples were crystallized. In this particular *s*-PP resin, three temperature regions for the observation of multiple-melting behavior are envisaged: (1) at low crystallization temperature region (i.e. $T_c <$ 40°C for both crystallization from the melt and glassy states), only the minor endotherm (located close to the corresponding crystallization temperature) and the high-temperature melting endotherm are observed; (2) at intermediate crystallization temperature region (i.e. $40 \leq T_c \leq 85$°C for both crystallization from the melt and glassy states), all of the three endotherms (i.e. the minor endotherm, the low-temperature melting endotherm and the high-temperature melting endotherm) are present; and (3) at high crystallization temperature region (i.e. $T_c >$ 85°C for both crystallization from the melt and glassy states), only the minor endotherm and the low-temperature melting endotherm are evident.

According to the above experimental observations, melting behavior of *s*-PP is characterized by the presence of three major endothermic peaks; they are (1) the minor endotherm (located close to the corresponding crystallization temperature T_c), (2) the low-temperature melting endotherm and (3) the high-temperature melting endotherm. Apparently, reading of the peak values of these endotherms (i.e. the minor peak temperature T_1, the low-melting peak temperature T_{ml} and the high-melting peak temperature T_{mh}, respectively) from the experimental data such as those presented in Figs. 3 and 4 is not going to be accurate. This can be alleviated by presenting the readings quantitatively in the form of tables, but inclusion of quantitative summary of these values along with the values of the enthalpy of fusion ΔH_f associated with these melting endotherms and the enthalpy of crystallization ΔH_c associated with crystallization exotherms was not warranted (by the reviewing board) for fear that the summary might appear to be a duplication of the graphical presentations of the data. Interested readers, however, are welcome to request for this summary from the corresponding author.

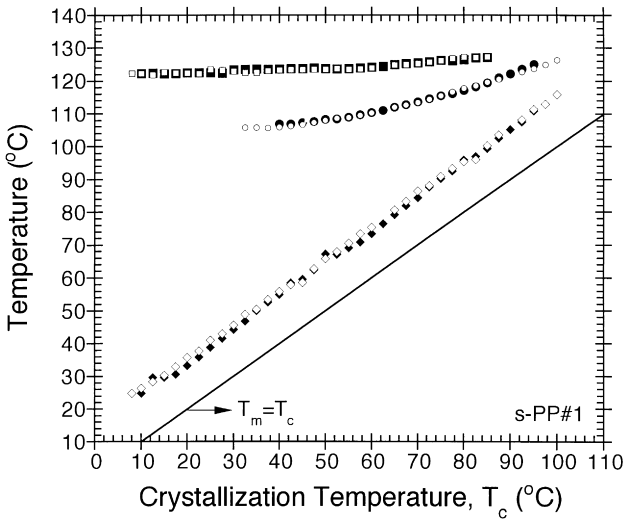

Fig. 5. Variation of the minor peak temperature T_1, the low-melting peak temperature T_{ml} and the high-melting peak temperature T_{mh}, as determined from the subsequent melting endotherms after complete crystallization from both the melt and glassy states, with the crystallization temperature T_c. Keys: (◆) (●) and (■) represent T_1, T_{ml}, T_{mh} values for crystallization from the melt states; (◇), (○) and (□) represent T_1, T_{ml}, T_{mh} values for crystallization from the glassy states, respectively.

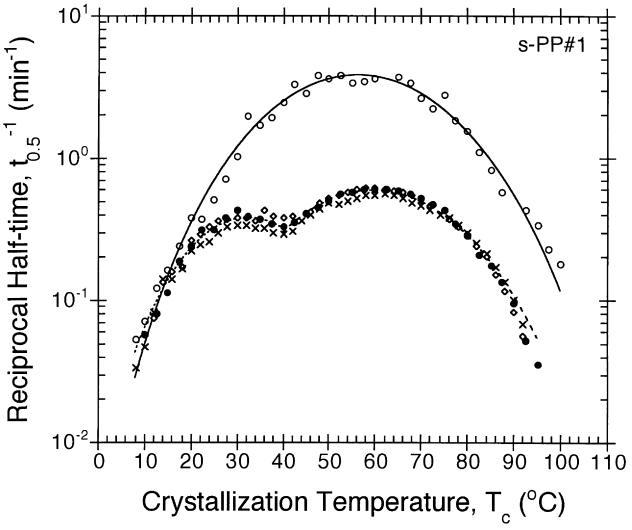

Fig. 6. Variation of the reciprocal half-time $t_{0.5}^{-1}$ as a function of crystallization temperature T_c: (◇) melt-crystallization data taken from Ref. [40]; (×) melt-crystallization data taken from Ref. [13]; (●) melt-crystallization data measured in this work; and (○) cold-crystallization data measured in this work. Different lines represent the best fits of the experimental data.

Fig. 5 illustrates plots of the minor peak temperature T_1, the low-melting peak temperature T_{ml} and the high-melting peak temperature T_{mh} as a function of the crystallization temperature T_c for both crystallization from the melt (shown as various filled geometrical points) and glassy states (shown as various unfilled geometrical points). According to Fig. 5, it is apparent that the minor peak temperature T_1 for both crystallization from the melt and glassy states increases steadily with increasing crystallization temperature. Interestingly, the difference between the values of the minor peak temperature T_1 and the corresponding crystallization temperature T_c is found to be nearly constant (i.e. $T_1 - T_c = 14.7 \pm 1.0$°C for melt-crystallization data; and $T_1 - T_c = 15.6 \pm 0.6$°C for cold-crystallization data). These findings are in parallel to what we found on *s*-PP#4 resin, in which $T_1 - T_c = 11.8 \pm 0.4$°C for melt-crystallization data (see Ref. [37, Fig. 3]). This confirms that melting always starts at a temperature close to the corresponding crystallization temperatures. It is also apparent, according to Fig. 5, that the low-melting peak temperature T_{ml} and the high-melting peak temperature T_{mh} exhibit a finite dependence on the crystallization temperature in an increasing manner, with the T_{ml} values being more dependent on T_c than the T_{mh} values are. It should be pointed out that the relation between T_{ml} and T_c exhibits a slight curvature.

According to our recent work [37], the minor endotherm represents the melting of the secondary crystallites formed at T_c. The low-temperature melting endotherm corresponds to the melting of the primary crystallites formed at T_c, while the high-temperature melting endotherm is attributed to the melting of the crystallites re-crystallized during a heating scan. Thus, the multiple-melting (triple-melting) behavior of *s*-PP observed in subsequent melting endotherms in DSC can be best described as contributions from: (1) melting of the secondary crystallites and their re-crystallization; (2) partial melting of the less stable fraction of the primary crystallites and their re-crystallization; (3) melting of the remaining fractions of the primary crystallites; and lastly (4) re-melting of the re-crystallized crystallites formed during the heating scan. It is important to note that the mechanisms and extent of the re-crystallization process during a heating scan depends greatly on the stability of the primary and secondary crystallites formed at T_c and on the heating rate used.

From the values of all of the peak temperatures (presented graphically in Fig. 5), it is interesting to note that even though the overall kinetics of the melt- and cold-crystallization processes is totally different, the peak temperatures of the low-temperature and high-temperature melting endotherms appear to be very comparable. This indicates that the lamellae formed at T_c either from the melt or glassy state should be of similar thickness, regardless of the difference in the nucleation mechanisms involved (see later). In other words, the lamellar thickness of the primary crystals appears to be mainly controlled by the crystallization temperature T_c (or to be exact, the degree of undercooling ΔT).

5. Discussion

5.1. Temperature dependence of overall crystallization kinetics parameters

The most fundamental representation of the overall

crystallization kinetics data is to plot the reciprocal value of the crystallization half-time (i.e. $t_{0.5}^{-1}$) as a function of the crystallization temperature T_c (see Fig. 6). If the crystallization half-time data can be collected with minimal degree of error over the whole temperature range (i.e. $T_g < T_c < T_m^0$), it is expected according to the secondary nucleation theory of Lauritzen and Hoffman (i.e. LH theory) [38,39], that the temperature dependence of the reciprocal half-time data (i.e. the plot of $t_{0.5}^{-1}$ versus T_c) should exhibit the typical bell-shaped curve, which can be described as a result of the nucleation control effect at low degrees of undercooling (i.e. high crystallization temperatures) and diffusion control effect at high degrees of undercooling (i.e. low crystallization temperatures).

According to Fig. 6, the plot of $t_{0.5}^{-1}$ versus T_c for $t_{0.5}$ data obtained from isothermal crystallization from the melt state (shown in Fig. 6 as filled circles) exhibit a "double" bell-shaped curve, while the similar plot for $t_{0.5}$ data obtained from isothermal crystallization from the glassy state (shown in Fig. 6 as open circles) exhibit the typical bell-shaped curve. In the case of isothermal crystallization from the melt state, the plots of $t_{0.5}^{-1}$ versus T_c for two other different data sets obtained from separate measurements (shown in Fig. 6 as open diamonds for data taken from Ref. [40] and as crosses for data taken from Ref. [13]) are also included. Interestingly, all of the data sets exhibit a distinct discontinuity in the plot of $t_{0.5}^{-1}$ versus T_c at a crystallization temperature T_c of ca. 40°C, which clearly separate the plot of $t_{0.5}^{-1}$ versus T_c into two bell-shaped curves. Since we have already proven that premature crystallization did not occur during sample transfer and thermal stabilization, the fact that excellent agreement is evident in the three data sets indicate that the observation of the double bell-shaped curve is definitely not an artefact, and, to the best of our knowledge, this is the first time that a double bell-shaped curve is observed in a plot of the overall crystallization rate as a function of crystallization temperature T_c.

According to the classical theories of the primary homogeneous nucleation rate I [41,42] and that of the secondary nucleation rate G (i.e. subsequent crystal growth rate) [38,39], the temperature dependence of I and G can be described by exponential equations of the form:

$$I = I_0 \exp\left[-\frac{U^*}{R(T_c - T_\infty)}\right]\exp\left[-\frac{K^l}{T_c(\Delta T)^2 f^2}\right], \qquad (9)$$

and

$$G = G_0 \exp\left[-\frac{U^*}{R(T_c - T_\infty)}\right]\exp\left[-\frac{K^G}{T_c(\Delta T) f}\right], \qquad (10)$$

where I_0 and G_0 are pre-exponential terms not strongly dependent on temperature, U^* is the activation energy for molecular segmental transport across the melt/solid interfacial boundary and is commonly given by a universal value of 6276 J mol^{-1} [38], R is the universal gas constant, T_∞ is the temperature where the long-range molecular motion ceases and is often taken to be ca. 50 K below the glass transition temperature (i.e. $T_\infty = T_g - 50$ K [38]), K^l and K^G are combined factors related to primary homogeneous nucleation and subsequent crystal growth mechanisms, respectively and f is a factor used to correct for the temperature dependence of the enthalpy of fusion (i.e. $f = 2T_c/(T_m^0 + T_c)$ [38]).

Referring to Eqs. (9) and (10), the first exponential term, i.e. $\exp(-U^*/R(T_c - T_\infty))$, corresponds to the diffusion of polymer molecules or segments of them from the equilibrium melt onto the growth face. The second exponential term, i.e. $\exp(-K^l/T_c(\Delta T)^2 f^2)$ in Eq. (9) or $\exp(-K^G/T_c(\Delta T)f)$ in Eq. (10), relates to the formation of the critical primary homogeneous and secondary nuclei, respectively. Owing to the competing contributions of the transport and nucleation terms, one expects that there should be a maximum in both of the primary homogeneous and crystal growth rate data at a temperature somewhere between the glass transition temperature T_g and the equilibrium melting temperature T_m^0, when plotted as a function of the crystallization temperature T_c. Indeed, maxima in the primary homogeneous and crystal growth rate data as a function of crystallization temperature are experimentally observed [43,44], with the maximum in the primary homogeneous nucleation rate data found at a lower temperature than that of the crystal growth rate data (see Ref. [44, Fig. 1]).

The finding by Okui [44] led us to believe that the observation of the two maxima in the plot of $t_{0.5}^{-1}$ versus T_c for $t_{0.5}$ data obtained from isothermal crystallization from the melt state is a result of the contributions from the maximum in the crystal growth rate at $T_{c,max}$ of about 60°C and from the maximum in the primary homogeneous nucleation rate at $T_{c,max} = 30$°C with a discontinuity being observed at $T_{c,break} = 40$°C. In contrast to the case of crystallization from the melt state, the plot of $t_{0.5}^{-1}$ versus T_c for $t_{0.5}$ data obtained from isothermal crystallization from the glassy state exhibits only one maximum at $T_{c,max} = 58$°C. We believe at this point that, for the crystallization from the melt state, the crystallization process is dominated by heterogeneous nucleation mechanisms until the crystallization temperature drops as low as $T_c = 60$°C, at which point the contribution from the primary homogeneous nucleation mechanisms start taking effect and increasingly dominates with further decrease in T_c (or further increase in the degree of undercooling ΔT).

Comparison of the overall crystallization rates measured from crystallization from the melt and glassy states (see Fig. 6) indicates that crystallization from the glassy state is much faster than that from the melt state. Since it is expected, based on the LH theory [38,39], that the crystal growth rate is only a function of crystallization temperature T_c, the fact that crystallization from the glassy state is much faster than that from the melt state must be attributable to the much higher contribution from the nucleation mechanisms (i.e., either as an increase in nucleation rate or nucleation density). In other words, the quenching

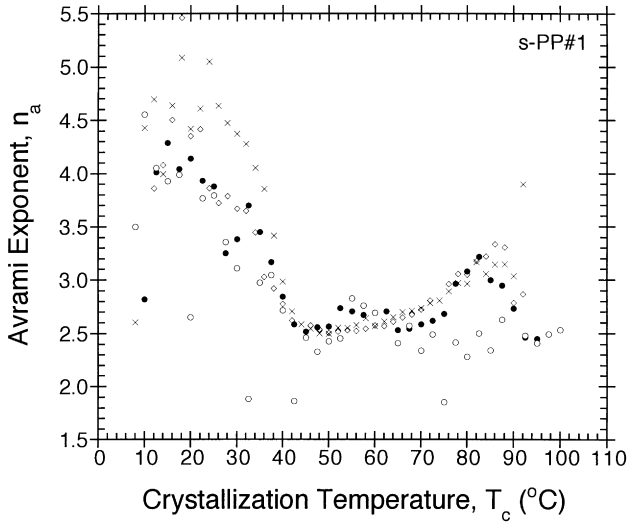

Fig. 7. Variation of the Avrami exponent n_a as a function of crystallization temperature T_c: (◇) melt-crystallization data taken from Ref. [40]; (×) melt-crystallization data taken from Ref. [13]; (●) melt-crystallization data measured in this work; and (○) cold-crystallization data measured in this work.

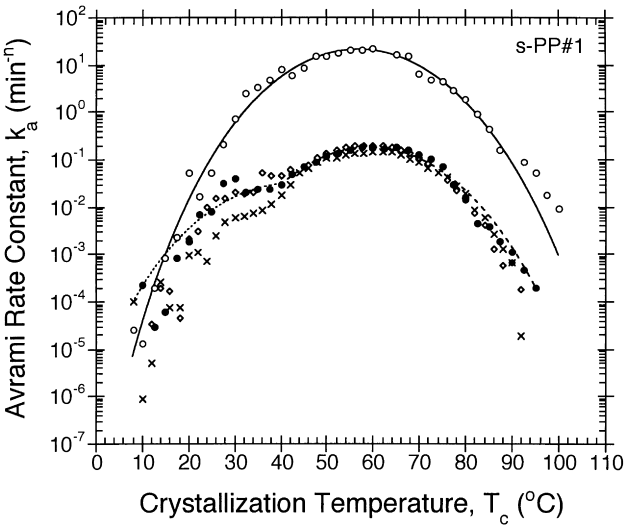

Fig. 9. Variation of the Avrami rate constant k_a as a function of crystallization temperature T_c: (◇) melt-crystallization data taken from Ref. [40]; (×) melt-crystallization data taken from Ref. [13]; (●) melt-crystallization data measured in this work; and (○) cold-crystallization data measured in this work. Different lines represent the best fits of the experimental data.

process tremendously increases the total number of activated nuclei and, upon crystallization at T_c, these activated nuclei can act as predetermined homogeneous nuclei (i.e. athermal nucleation mechanism) which greatly enhance the overall crystallization rate [45].

Let us now consider the temperature dependence of other kinetics parameters determined based on the Avrami and Malkin macrokinetic models (see Eqs. (1) and (2)). Figs. 7 and 8 illustrate plots of the Avrami and Malkin exponents for crystallization from the melt and glassy states as a function of crystallization temperature, respectively. For crystallization from the melt state, both the Avrami and Malkin exponents exhibit a similar temperature dependence. Clearly, the temperature dependence of these parameters can be divided into two regions: (1) "low" temperature region (i.e. $10 \leq T_c \leq 40$°C); and (2) "moderate" temperature region (i.e. $40 \leq T_c \leq 95$°C). In the moderate temperature region, values of both the Avrami and Malkin exponents increase with increasing crystallization temperature, with a maximum being observed at $T_c = 87.5$°C. In the low-temperature region, values of both the Avrami and Malkin exponents increase monotonically with decreasing

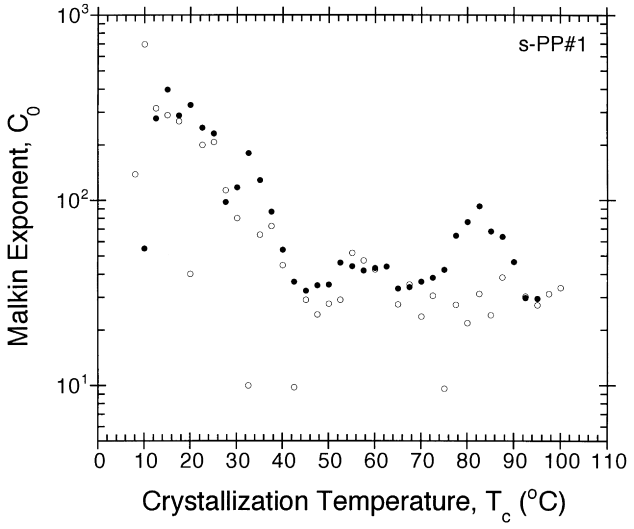

Fig. 8. Variation of the Malkin exponent C_0 as a function of crystallization temperature T_c: (●) melt-crystallization data measured in this work; and (○) cold-crystallization data measured in this work.

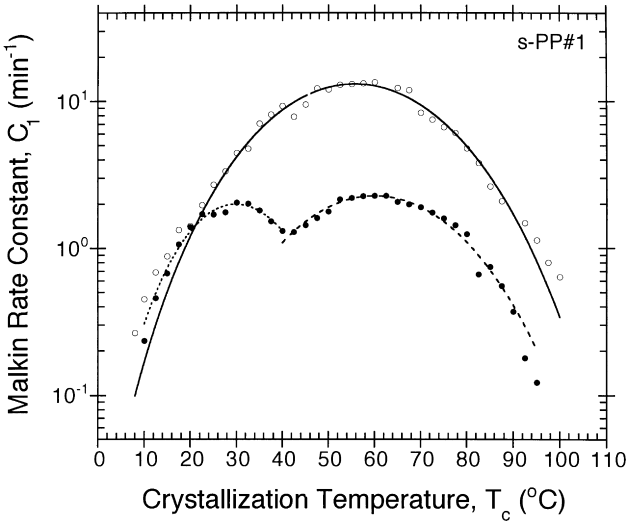

Fig. 10. Variation of the Malkin rate constant C_1 as a function of crystallization temperature T_c: (◇) melt-crystallization data taken from Ref. [40]; (×) melt-crystallization data taken from Ref. [13]; (●) melt-crystallization data measured in this work; and (○) cold-crystallization data measured in this work. Different lines represent the best fits of the experimental data.

Table 1
The fitting parameters, provided by the non-linear multi-variable regression program, for the best possible fits of the respective bulk crystallization rate parameters (e.g. $t_{0.5}^{-1}$, k_a, C_1 and $k_a^{1/n}$) according to Eq. (13)

Ψ	Ψ_0	Θ (cal mol^{-1})	K (K^2)	r^2
For melt-crystallization data in the range 10 ≤ T_c ≤ 40°C				
$t_{0.5}^{-1}$ (min^{-1})	1.56×10^{21}	867.5	1.48×10^{6}	0.9662
$k_a^{1/n}$ (min^{-1})	7.80×10^{21}	878.4	1.53×10^{6}	0.9707
k_a (min^{-n})	1.09×10^{22}	1650.4	1.45×10^{6}	0.7595
C_1 (min^{-1})	4.42×10^{30}	1041.5	2.12×10^{6}	0.9776
For melt-crystallization data in the range 40 ≤ T_c ≤ 95°C				
$t_{0.5}^{-1}$ (min^{-1})	4.82×10^{9}	1301.2	4.98×10^{5}	0.9889
$k_a^{1/n}$ (min^{-1})	3.26×10^{9}	1289.1	4.92×10^{5}	0.9889
k_a (min^{-n})	7.08×10^{26}	3590.7	1.39×10^{6}	0.9726
C_1 (min^{-1})	3.40×10^{10}	1351.4	5.09×10^{5}	0.9784
For cold-crystallization data				
$t_{0.5}^{-1}$ (min^{-1})	7.04×10^{9}	1082.0	4.89×10^{5}	0.9851
$k_a^{1/n}$ (min^{-1})	9.83×10^{9}	1085.8	4.92×10^{5}	0.9885
k_a (min^{-n})	4.09×10^{28}	3260.0	1.43×10^{6}	0.9872
C_1 (min^{-1})	4.22×10^{10}	1087.7	5.05×10^{5}	0.9799

crystallization temperature. Interestingly, the temperature dependence of the Avrami and Malkin exponents for crystallization from the glassy state appears to be similar to what is observed for the case of crystallization from the melt state. A slight difference can be seen in the moderate temperature region where both of the Avrami and Malkin exponents appear to be unaffacted by changes in the crystallization temperature. The majority of the exponents found for crystallization from the glassy state observed in this range appears to be smaller than those found for crystallization from the melt state (especially, within the T_c range of ca. 60 to 90°C). According to the classical definition of the Avrami exponent [35], the nucleation mechanisms in crystallization from the glassy state are more instantaneous in time than those in crystallization from the melt state.

Figs. 9 and 10 show plots of the Avrami and Malkin rate constants (i.e. k_a and C_1, respectively) for crystallization from the melt and glassy states as a function of crystallization temperature. In general, the temperature dependence of these parameters is in accordance with the experimental observation made earlier on the reciprocal values of the crystallization half-time (i.e. $t_{0.5}^{-1}$). This is not surprising, however, since both of the Avrami and Malkin rate constants relate directly to the values of the reciprocal half-time $t_{0.5}^{-1}$ data according to the following equations:

$$k_{a,calc} = \ln 2\cdot(t_{0.5}^{-1})^{n_a}, \tag{11}$$

and

$$C_{1,calc} = \ln(4^{n_a} - 2)\cdot(t_{0.5}^{-1}). \tag{12}$$

We have also calculated the Avrami and Malkin rate constants according to Eqs. (11) and (12) and have found that the difference between the experimental values and the calculated values (not shown) is lower than 3% on average.

Since the overall crystallization rate parameters (e.g. $t_{0.5}^{-1}$, k_a and C_1) relate, in one way or another, to the primary homogeneous nucleation rate I and/or the subsequent crystal growth rate G and since the temperature dependence of these microscopic mechanisms are well defined in the literature [38,39,41,42] as discussed previously, the temperature dependence of the overall rate parameter can accordingly be quantified and described. Even though the temperature dependence of the parameters I and G are known to have a different temperature dependence (see Eqs. (9) and (10), respectively), the overall rate parameters have often been taken to have a similar temperature dependence to that of the crystal growth rate G. According to this approximation, the temperature dependence of the overall crystallization rate data (e.g. $t_{0.5}^{-1}$, k_a and C_1) can therefore be written as

$$\Psi(T_c) = \Psi_0 \exp\left[-\frac{\Theta}{R(T_c - T_\infty)}\right]\exp\left[-\frac{K_3^G}{T_c(\Delta T)f}\right], \tag{13}$$

where $\Psi(T_c)$ and Ψ_0 are respective overall crystallization rate parameters (e.g. $t_{0.5}^{-1}$, k_a and C_1) and pre-exponential parameters (e.g. $(t_{0.5}^{-1})_0$, k_{a0} and C_{10}), respectively, Θ is a parameter related to the activation energy characterizing the molecular transport across the melt/solid interface, K_3^G is a combined factor related to the secondary nucleation mechanisms and other quantities are the same as previously defined. It is also interesting to determine whether or not the overall rate parameters can be taken at a similar temperature dependence to that of the primary homogeneous nucleation rate I. According to such an approximation, the temperature dependence of the overall crystallization rate data (e.g. $t_{0.5}^{-1}$, k_a and C_1) may be described by

$$\Psi(T_c) = \Psi_0 \exp\left[-\frac{\Theta}{R(T_c - T_\infty)}\right]\exp\left[-\frac{K_4^I}{T_c(\Delta T)^2 f^2}\right], \tag{14}$$

where K_4^I is a combined factor related to the primary nucleation mechanisms, and other quantities are the same as previously defined.

According to Eqs. (13) and (14), temperature dependence of the overall rate function $\Psi(T_c)$ can now be quantified by directly fitting the respective overall crystallization rate parameters (e.g. $t_{0.5}^{-1}$, k_a and C_1) collected at various crystallization temperatures to one of the equations using the same non-linear multi-variable regression program. In order to obtain the best possible fits for the respective overall crystallization rate data, two input parameters have to be predefined: (1) the glass transition temperature, T_g = ca. − 6°C or ca. 267 K [14]; and (2) the equilibrium melting temperature, T_m^0 = ca. 168.7°C [14]. In doing so, the only unknown parameters that are provided by the program, once the best was determined, are Ψ_0, Θ, K_3^G and K_4^I. The corresponding best fits for all of the overall crystallization rate data (e.g. $t_{0.5}^{-1}$, k_a and C_1) are also shown in Figs. 6, 9 and 10 as different lines; whereas, the values of the Ψ_0, Θ, K_3^G and K_4^I as the result of the best fits according to Eqs. (13) and

Table 2
The fitting parameters, provided by the non-linear multi-variable regression program, for the best possible fits of the respective bulk crystallization rate parameters (e.g. $t_{0.5}^{-1}$, k_a, C_1 and $k_a^{1/n}$) according to Eq. (14)

Ψ	Ψ_0	Θ (cal mol^{-1})	K (K^2)	r^2
For melt-crystallization data in the range $10 \le T_c \le 40$°C				
$t_{0.5}^{-1}$ (min^{-1})	1.55×10^{9}	1029.5	5.53×10^{7}	0.9664
$k_a^{1/n}$ (min^{-1})	2.73×10^{9}	1046.3	5.73×10^{7}	0.9708
k_a (min^{-n})	2.25×10^{10}	1817.5	5.47×10^{7}	0.7595
C_1 (min^{-1})	2.63×10^{13}	1273.2	7.92×10^{7}	0.9890
For melt-crystallization data in the range $40 \le T_c \le 95$°C				
$t_{0.5}^{-1}$ (min^{-1})	1.01×10^{5}	1232.8	1.63×10^{7}	0.9900
$k_a^{1/n}$ (min^{-1})	7.67×10^{4}	1220.7	1.61×10^{7}	0.9900
k_a (min^{-n})	1.66×10^{14}	3492.8	4.71×10^{7}	0.9732
C_1 (min^{-1})	5.39×10^{5}	1276.7	1.66×10^{7}	0.9902
For cold-crystallization data				
$t_{0.5}^{-1}$ (min^{-1})	3.11×10^{5}	1072.8	1.66×10^{7}	0.9848
$k_a^{1/n}$ (min^{-1})	2.84×10^{5}	1077.0	1.67×10^{7}	0.9883
k_a (min^{-n})	9.95×10^{15}	3231.9	4.92×10^{7}	0.9879
C_1 (min^{-1})	1.41×10^{6}	1082.5	1.73×10^{7}	0.9903

(14) are summarized in Table 1 for the melt-crystallization data and in Table 2 for the cold-crystallization data. It should be noted the dashed line in each figure represents the best fit to the melt-crystallization data in the range of $40 \le T_c \le 95$°C, the dotted line represents the best fit to the melt-crystallization data in the range of $10 \le T_c \le 40$°C, and the solid line represents the best fit to the cold-crystallization data.

Before going further into the discussion of the thermodynamic melting temperature, we would like to establish a comment on a common use of an Arrhenius temperature dependence in describing the temperature dependence of the Avrami rate constant k_a (see, for examples, Refs. [46–49]), which reads

$$(k_a)^{1/n_a} = (k_a)_0 \exp\left(-\frac{\Delta E_0}{RT_c}\right), \tag{15}$$

where $(k_a)_0$ is a temperature-independent pre-exponential parameter, ΔE_0 is the effective activation energy describing the overall crystallization kinetics and others variables are the same as previously defined. Apparently, a linear relation is expected when a plot of $(1/n_a)$ ln k$_a$ versus T_c^{-1} (the unit of T_c is in [K]) is performed, in which the slope is then used to determine the activation energy ΔE_0. A number of investigators [46–49] claimed to observe a linear relation in the plot of $(1/n_a)$ ln k$_a$ versus T_c^{-1}. It should be noted however that in those reports [46–49] the Avrami rate constant k_a data used to construct the plot were collected within a small range of crystallization temperatures T_c (i.e. <10°C).

Fig. 11 illustrates plots of $(1/n_a)$ ln k$_a$ versus T_c^{-1} for the k_a data collected over a wide T_c range. Instead of observing a linear relation in each of the plots, we arrive at plots similar to those of the reciprocal half-time $t_{0.5}^{-1}$ versus the crystallization temperature T_c (see Fig. 6). This is not surprising, however, since the Avrami rate constant k_a is known to

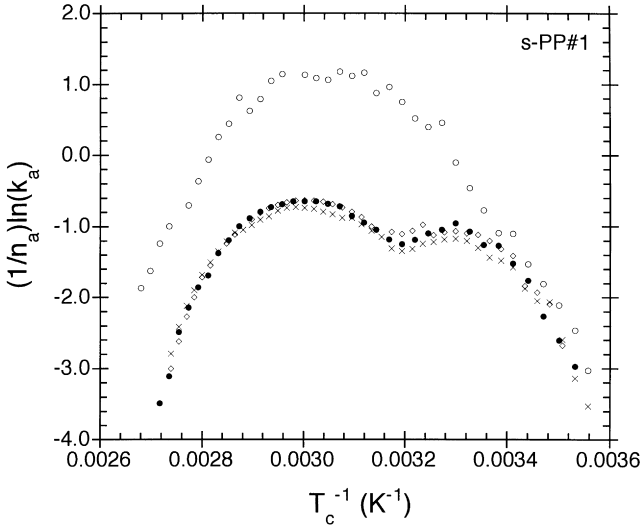

Fig. 11. Variation of $(1/n_a)$ ln k_a as a function of the inversed crystallization temperature T_c^{-1} according to Eq. (15). Keys: (◇) melt-crystallization data taken from Ref. [40]; (×) melt-crystallization data taken from Ref. [13]; (●) melt-crystallization data measured in this work; and (○) cold-crystallization data measured in this work.

relate to the reciprocal half-time $t_{0.5}^{-1}$ according to Eq. (11). To demonstrate this fact, we plotted $k_a^{1/n}$ as a function of the crystallization temperature T_c (not shown), and fitted the plots according to Eqs. (13) and (14) using the non-linear multi-variable regression program. The values of Ψ_0, Θ, K_3^G and K_4^I as the result of the best fits according to Eqs. (13) and (14) are also summarized in Tables 1 and 2, respectively. Evidently, the resulting fitting parameters are comparable to those obtained from the plots of $t_{0.5}^{-1}$ versus T_c.

The results we illustrated in Fig. 11 apparently indicate that Eq. (15) cannot and should not be used to describe the temperature dependence of the Avrami rate constant k_a. It is important to note that when a set of experimental data is collected over a small T_c range as being carried out in the referenced reports [46–49], a slight curvature observed in the plot of $(1/n_a)$ ln k$_a$ versus T_c^{-1} can be easily misled as a linear dependence (see, for example, Ref. [47, Fig. 3] and Ref. [48, Fig. 4]), and the degree of the curvature depends on the T_c range in which one is carried out his experiment. Consequently, the ΔE_0 value determined from the plot of $(1/n_a)$ ln k$_a$ versus T_c^{-1} is not a constant, as it clearly depends on the range of the data used in the construction of the plot. Since the ΔE_0 value is not a constant (for a polymer system), use of the ΔE_0 values to compare the overall crystallization kinetics of different polymer systems is clearly meaningless.

5.2. Determination of the equilibrium melting temperature

We discussed in our earlier report [37] that the values of the low-melting peak temperature T_{ml} correspond to the melting of the primary crystals formed at a specified T_c, thus the observed T_{ml} values are now considered as the melting points T_m of the crystalline aggregates formed in

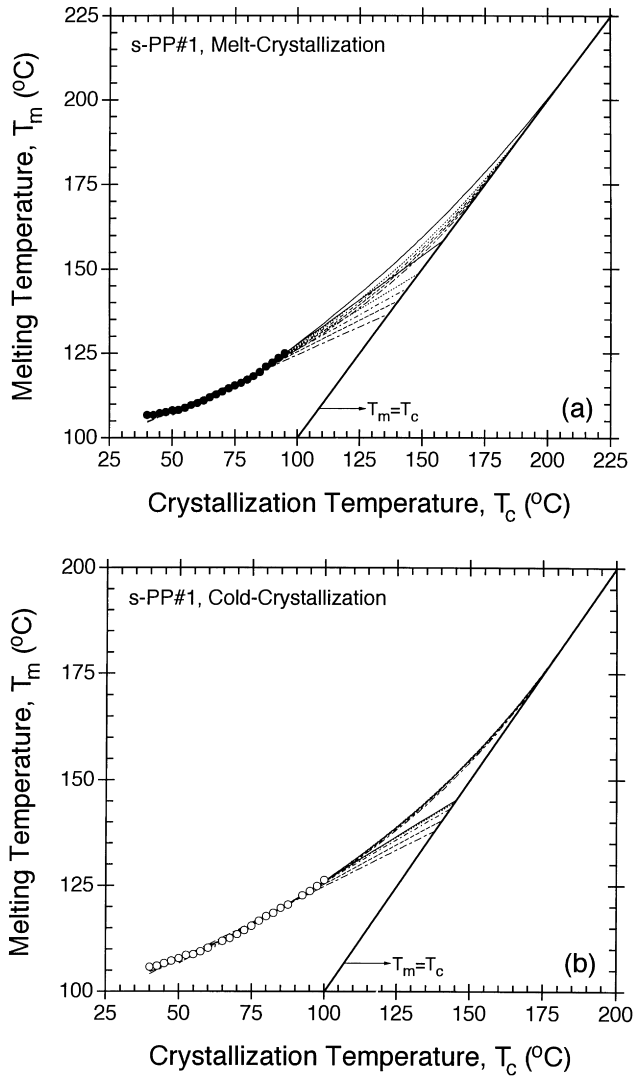

Fig. 12. Variation of the low-melting peak temperature T_{ml} (or the melting temperature T_m of the primary crystals formed at T_c) as a function of the crystallization temperature T_c for: (a) isothermal crystallization from the melt state (●); and (b) isothermal crystallization from the glassy state (○), and corresponding linear and non-linear Hoffman–Weeks extrapolations shown as straight and curved lines, respectively. Keys: (– · –) fitted line for the data range $40 \le T_c \le 95$°C; (– – –) fitted line for the data range $50 \le T_c \le 95$°C; (– · – · ·) fitted line for the data range $60 \le T_c \le 95$°C; (· · ·) fitted line for the data range $70 \le T_c \le 95$°C; and (—) fitted line for the data range $80 \le T_c \le 95$°C.

the samples after complete crystallization from the melt and glassy states at T_c. According to a theory derived by Hoffman and Weeks [50], the equilibrium melting temperature T_m^0 (i.e. the melting temperature of infinitely extended crystals) can be obtained by linear extrapolation of observed T_m–T_c data to the line $T_m = T_c$. Mathematically, they arrived at the following equation (hereafter called the "linear" Hoffman–Weeks extrapolation (LHW)):

$$T_m = \frac{T_c}{2\beta} + T_m^0\left[1 - \frac{1}{2\beta}\right], \tag{16}$$

where β is the "thickening ratio". In other words, β indicates the ratio of the thickness of the mature crystal l_c to that of the initial one l_c^*; therefore, $\beta = l_c/l_c^*$, which is supposed to always be greater than or equal to 1. It should be noted that the factor 2 in Eq. (16) suggests that the thickness of the crystals undergoing melting is approximately double that of the initial critical thickness [51].

Fig. 12a and b shows plots of T_{ml} (or the observed T_m value of the crystallites formed at T_c) as a function of crystallization temperature T_c for the data taken from melt- and cold-crystallization, respectively. It is evident that a slightly upward curvature is discernable in both sets of data. Intuitively, it is obvious that the value of the equilibrium melting temperature T_m^{LHW} determined from linear extrapolation of the observed T_m–T_c data to the line $T_m = T_c$ will depend significantly on the range of the data used in the extrapolation (due to the curvature of the data). In this present work, we divide the observed T_m–T_c data into five regions accordingly (see Table 3). Within each region, a linear Hoffman–Weeks extrapolation is performed (also shown in Fig. 12a and b as different linear lines) and the corresponding values of the equilibrium melting temperature T_m^{LHW}, the lamellar thickening ratio β (i.e. $\beta = 0.5 \times \text{slope}^{-1}$) and the correlation coefficient r^2 (justifying the goodness of the fit) are reported in Table 3. It is obvious, according to Table 3, that the resulting T_m^{LHW} and β values depend greatly on the range of the observed T_m–T_c data used in the extrapolation.

According to the basis of the linear Hoffman–Weeks extrapolative method, the extrapolated T_m^{LHW} value is only valid when the resulting thickening ratio β (calculated from the slope of the linear extrapolation) is equal to or close to 1. As a result, the equilibrium melting temperature T_m^{LHW} determined from the observed T_m–T_c data should lie between 148.7 and 158.2°C in the case of crystallization from the melt state, and should be higher than 145.3°C in the case of crystallization from the glassy state. Let us pay a closer consideration to the curvature of the observed T_m–T_c data. If it is possible to extend the data range into the higher crystallization temperature region and if the primary crystallites formed at those temperatures do not severely thicken (the probability for crystal thickening increases tremendously with increasing crystallization temperature), it is hypothesized that the observed T_m values should follow the common curvature of the observed T_m–T_c data shown in Fig. 12a and b and it should intersect with the line $T_m = T_c$ at the true equilibrium melting temperature T_m^0 of this *s*-PP resin. If this hypothesis is valid, no matter what data range one chooses to perform the linear Hoffman–Weeks extrapolation the T_m^{LHW} value obtained will not represent the true equilibrium melting temperature T_m^0 and will always be lower (i.e. $T_m^{LHW} < T_m^0$). However, the closer is the range of the data to the true equilibrium melting temperature T_m^0, the smaller is the difference between the true and the extrapolated values (one has to make sure that the observed T_m values obtained at high T_c do not represent the melting temperature of the thickened crystallites formed at that temperature).

Table 3
Summary of the equilibrium melting temperature T_m^{LHW} and the lamellar thickening ratio β as suggested by the linear Hoffman–Weeks extrapolative method, and the equilibrium melting temperature T_m^{NLHW} and the parameter a associated with the resulting T_m^{NLHW} value as suggested by the non-linear Hoffman–Weeks extrapolative method for the observed T_m–T_c data ranges specified

T_m–T_c data range	T_m^{LHW} (°C)	β	r^2	T_m^{NLHW} (°C)	a	r^2
For melt-crystallization data						
$40 \le T_c \le 95$°C	136.6	1.5	0.982	178.0	2.90	0.984
$50 \le T_c \le 95$°C	140.6	1.3	0.991	183.3	2.55	0.991
$60 \le T_c \le 95$°C	144.3	1.2	0.994	188.2	2.28	0.993
$70 \le T_c \le 95$°C	148.7	1.1	0.994	194.4	2.00	0.992
$80 \le T_c \le 95$°C	158.2	0.9	0.999	210.2	1.47	0.998
For cold-crystallization data						
$40 \le T_c \le 100$°C	137.9	1.5	0.992	177.3	2.93	0.997
$50 \le T_c \le 100$°C	140.4	1.3	0.996	179.7	2.76	0.998
$60 \le T_c \le 100$°C	143.2	1.2	0.999	181.8	2.61	0.999
$70 \le T_c \le 100$C	144.7	1.2	0.999	182.1	2.59	0.999
$80 \le T_c \le 100$°C	145.3	1.2	0.998	180.9	2.67	0.998

We have already mentioned that a slightly upward curvature is apparent in both sets of data (see Fig. 12a and b). This upward curvature in the observed T_m–T_c data had also been observed in various other polymer systems (see, for example, Refs. [51,52]), thus raising a concern on the assumed constancy of the thickening ratio β. In fact, Weeks [53] pointed out long ago that the increase in observed T_m value with increasing crystallization time is a result of the increase in lamellar thickness, which has a logarithmic dependence on time (although this remark should only be valid for polymers which exhibit significant α-relaxation, e.g. linear PE and *i*-PP). This simply means that the thickening effect is much more severe at higher T_c values (as a result of a combination of high molecular mobility and small relaxation time of the amorphous layer) where prolonged crystallization time is needed for complete crystallization.

Although the non-linearity in the observed T_m–T_c data over a wide range of temperature was explained to some extent by Alamo et al. [51], it is the recent contribution by Marand et al. [54] that offers a new method of determining the T_m^0 value based on the observed T_m–T_c data in which the observed T_m data were taken from samples crystallized at different temperatures but with the same a priori lamellar thickening coefficient. Derived based on the Gibbs–Thomson equation [38,55] and on the proposition of Lauritzen and Passaglia [56] on stem length fluctuation during chain folding, Marand et al. [54] proposed a new mathematical derivation which states a relationship between the observed melting temperature and the corresponding crystallization temperature. This equation is hereafter called the "non-linear" Hoffman–Weeks extrapolation (NLHW), and is given in the form:

$$\frac{T_m^0}{T_m^0 - T_m} = \beta^m \frac{\sigma_e^1}{\sigma_e^{GT}} \left[\frac{T_m^0}{T_m^0 - T_c} + \frac{D_2 \Delta H_f^0}{2\sigma_e^1} \right], \tag{17a}$$

or in a simpler form:

$$M = \beta^m \frac{\sigma_e^1}{\sigma_e^{GT}} (X + a), \tag{17b}$$

where β^m is the thickening coefficient (see β in Eq. (16)), σ_e^{GT} is the basal interfacial free energy associated with nuclei of critical size including the extra lateral surface energy due to fold protrusion and the mixing entropy associated with stems of different lengths (σ_e^{GT} is the basal interfacial free energy as appeared in the Gibbs–Thomson equation [38,55]), σ_e^1 is the interfacial energy associated with the formation of the basal plane of the initial crystals which can be estimated from the slope of a plot of the lamellar thickness versus the inverse degree of undercooling (i.e. l_c^* versus ΔT^{-1}), D_2 is a constant and all other parameters are the same as previously defined. It is worth noting that for most cases it is safe to assume that $\sigma_e^1 \approx \sigma_e^{GT}$, [54]. Precautionary remarks regarding the use of the non-linear Hoffman–Weeks procedure to estimate the equilibrium melting temperature T_m^0 were addressed in detail in the original publication by Marand et al. [54].

In order to apply Eq. (17) to analyze the observed T_m–T_c data in real polymer systems, it is required that the observed T_m data be collected from samples crystallized at different temperatures but having the same lamellar thickening coefficient β^m. For each set of the observed T_m–T_c data, corresponding values of M and X in Eq. (16) can be calculated for a given choice of the equilibrium melting temperature T_m^0. In case of $\sigma_e^1 = \sigma_e^{GT}$, the "actual" equilibrium melting temperature T_m^0 is taken as the seed T_m^0 value which results in the plot of M versus X being a straight line with slope of unity (i.e. $\beta^m = 1$) and intercept of a (i.e. $a = D_2 \Delta H_f^0 / 2\sigma_e^1$). Since it had been shown in the case of *s*-PP that lamellar thickening does not occur during isothermal crystallization, at least within the crystallization temperature range studied [37,57,58], we can reasonably assume that the observed T_m data obtained were collected from lamellae having the same thickening coefficient β^m, thus enabling them to be analyzed using this method.

In each of the five regions of the observed T_m–T_c data, a non-linear Hoffman–Weeks extrapolation is performed (also shown in Fig. 12a and b as different curve lines) according to the procedure described in the previous paragraph. The resulting values of the equilibrium melting temperature T_m^{NLHW}, the parameter a associated with the resulting T_m^{NLHW} value, and the correlation coefficient r^2 are summarized in Table 3. It is apparent, according to Table 3, that the resulting T_m^{NLHW} and a values determined from the melt-crystallization data depend greatly on the range of the observed T_m–T_c data used in the extrapolation; whereas, those determined from the cold-crystallization data do not vary significantly. Comparison of values of the correlation coefficient r^2 summarized in Table 3 indicates that the observed T_m–T_c data obtained from crystallization from the melt state are much more scattered than

those obtained from crystallization from the glassy state, and this should be the reason for the large variation observed in the resulting T_m^{NLHW} values determined from the melt-crystallization data. If we are to assume that the lamellar thickness is only a function of crystallization temperature T_c (or to be exact, the degree of undercooling ΔT) regardless of the nucleation mechanisms involved, one should be able to determine the true equilibrium melting temperature T_m^0 of the polymer of interest from either melt- or cold-crystallization experiment. If the aforementioned assumption is valid, the true equilibrium melting temperature T_m^0 of this *s*-PP resin should be taken as $T_m^{NLHW} = 181.8°C$ (judged from the lowest value of the correlation coefficient r^2 of the fit) and the parameter a associated with this T_m^{NLHW} value is 2.61.

6. Conclusions

In this manuscript, DSC was used to investigate the overall kinetics of melt- and cold-crystallization of *s*-PP under isothermal quiescent conditions and subsequent melting behavior. A non-linear multi-variable regression program was used to fit the isothermal crystallization measurements obtained from the DSC according to Avrami and Malkin macrokinetic models. The crystallization kinetics parameters specific to each of the model were obtained along with the best fits, provided by the program.

For crystallization from the melt state, all of the crystallization rate parameters considered (e.g. $t_{0.5}^{-1}$, k_a and C_1) exhibit an unmistakable double bell-shaped curve when plotted as a function of crystallization temperature T_c, with the two maxima being observed at T_c of ca. 30 and ca. 60°C owing to the contributions from the maximum in the crystal growth rate and from the maximum in the primary nucleation rate, respectively, and the discontinuity being observed at T_c of ca. 40°C. For crystallization from the glassy state however, the typical bell-shaped curve is observed when all of the crystallization rate parameters considered (e.g. $t_{0.5}^{-1}$, k_a and C_1) were plotted as a function of crystallization temperature T_c, with a maximum being observed at T_c of ca. 58°C. Comparison of the crystallization rate parameters (e.g. $t_{0.5}^{-1}$, k_a and C_1) measured from both melt- and cold-crystallization processes indicate that crystallization from the glassy state proceeds in a much faster rate than that from the melt state. This clearly suggests that quenching process greatly increases the total number of activated nuclei (or the rate of formation of the nuclei) and, upon subsequent crystallization at T_c, these activated nuclei can act as predetermined homogeneous nuclei that tremendously enhance the overall crystallization rate.

The multiple-melting (triple-melting) behavior of *s*-PP observed in subsequent melting endotherms in DSC can be explained as the contributions from: (1) melting of the secondary crystallites and their re-crystallization; (2) partial melting of the less stable fraction of the primary crystallites and their re-crystallization; (3) melting of the remaining fractions of the primary crystallites; and lastly (4) re-melting of the re-crystallized crystallites formed during the heating scan. The observation and strength of the high-temperature melting endotherm is found to depend strongly on the stability of the secondary and the primary crystallites formed and on the scanning rate used to observe the melting behavior.

Lastly, analysis of the low-melting temperature according to the linear and non-linear Hoffman–Weeks extrapolative methods to obtain the equilibrium melting temperature T_m^0 is found to be somewhat sensitive to the range of the observed T_m–T_c data within which the extrapolations were carried out and perhaps to the accuracy of the data obtained. The results also suggest that the linear Hoffman–Weeks extrapolation always underestimate the value of the equilibrium melting temperature. As a result, the equilibrium melting temperature T_m^{NLHW} determined from the non-linear Hoffman–Weeks extrapolation may be taken as the better estimate of the true equilibrium melting temperature T_m^0 for this *s*-PP resin (i.e. $T_m^0 \cong T_m^{NLHW} = 181.8°C$). However, the accuracy of the estimate is still unclear, at least for the case of *s*-PP.

Acknowledgements

We would like to thank Dr Joseph Schardl of Fina Oil and Chemical Company, Dallas, TX for donating the *s*-PP resin used in this study, and Dr Roger A. Phillips and his co-workers of Montell USA, Inc., Elkton, MD for performing molecular characterizations of the resin.

References

[1] Natta G, Pasquon I, Corradini P, Peraldo M, Pegoraro M, Zambelli A. Rend Acd Naz Lincei 1960;28:539.
[2] Natta G, Pasquon I, Zambelli A. J Am Chem Soc 1962;84:1488.
[3] Ewen JA, Johns RL, Razavi A, Ferrara JD. J Am Chem Soc 1988;110:6255.
[4] Schardl J, Sun L, Kimura S, Sugimoto R. SPE-ANTEC Proc 1995:3414.
[5] Schardl J, Sun L, Kimura S, Sugimoto R. J Plastic Film Sheeting 1996;12:157.
[6] Sun L, Shamshoum E, DeKunder G. SPE-ANTEC Proc 1996:1965.
[7] Gownder M. SPE-ANTEC Proc 1998:1511.
[8] Sura RK, Desai P, Abhiraman AS. SPE-ANTEC Proc 1999:1764.
[9] Wheat WR. SPE-ANTEC Proc 1995:2275.
[10] Wheat WR. SPE-ANTEC Proc 1997:565.
[11] Rodriguez-Arnold J, Bu Z, Cheng SZD. J Macromol Sci-Rev Macromol Chem Phys 1995;C35:117.
[12] Rodriguez-Arnold J, Zhang A, Cheng SZD, Lovinger AJ, Hsieh ET, Chu P, Johnson TW, Honnell KG, Geerts RG, Palackal SJ, Hawley GR, Welch MB. Polymer 1994;35:1884.
[13] Supaphol P, Hwu JJ-J, Phillips PJ, Spruiell JE. SPE-ANTEC Proc 1997:1759.
[14] Supaphol P, Spruiell JE. J Appl Polym Sci 2000;75(1):44.
[15] Rodriguez-Arnold J, Bu Z, Cheng SZD, Hsieh ET, Johnson TW, Geerts RG, Palackal SJ, Hawley GR, Welch MB. Polymer 1994;35:5194.

[16] Supaphol P, Spruiell JE. Polymer 2000;41(3):1205.
[17] Bu Z, Yoon Y, Ho R-M, Zhou W, Jangchud I, Eby RK, Cheng SZD, Hsieh ET, Johnson TW, Geerts RG, Palackal SJ, Hawley GR, Welch MB. Macromolecules 1996;29:6575.
[18] Vancso GJ, Beekmans LGM, Trifonova D, Varga J. ACS-PMSE Prepr 1999;81:232.
[19] Taguchi K, Miyaji H, Izumi K, Hoshino A, Miyamoto Y, Kokawa R. ACS-PMSE Prepr 1999;81:308.
[20] Keith HD, Padden FJ. J Appl Phys 1964;35:1270.
[21] Keith HD, Padden FJ. J Appl Phys 1964;35:1286.
[22] Verma R, Marand H, Hsiao B. Macromolecules 1996;29:7767.
[23] Marand H, Alizadeh A. ACS-PMSE Prepr 1999;81:238.
[24] Kolmogoroff AN. Izvestiya Akad Nauk USSR, Ser Math 1937;1:355.
[25] Johnson WA, Mehl KF. Trans Am Inst Mining Met Engng 1939;135:416.
[26] Avrami M. J Chem Phys 1939;7:1103.
[27] Avrami M. J Chem Phys 1940;8:212.
[28] Avrami M. J Chem Phys 1941;9:177.
[29] Evans UR. Trans Faraday Soc 1945;41:365.
[30] Tobin MC. J Polym Sci, Polym Phys 1974;12:399.
[31] Tobin MC. J Polym Sci, Polym Phys 1976;14:2253.
[32] Tobin MC. J Polym Sci, Polym Phys 1977;15:2269.
[33] Malkin AY, Beghishev VP, Keapin IA, Bolgov SA. Polym Engng Sci 1984;24:1396.
[34] Supaphol P, Spruiell JE. J Macromol Sci — Phys B 2000;39(2):257.
[35] Wunderlich B. Macromolecular physics, vol. 2. New York: Academic Press, 1976. p. 132–47.
[36] Supaphol P, Spruiell JE. J Appl Polym Sci 2000;75(3):337.
[37] Supaphol P. J Appl Polym Sci (subm.).
[38] Hoffman JD, Davis GT, Lauritzen Jr. JI. In: Hannay NB, editor. Treatise on solid state chemistry, vol. 3. New York: Plenum, 1976 (Chap. 7).
[39] Hoffman JD, Miller RL. Polymer 1997;38:3151.
[40] Supaphol P. Unpublished research.
[41] Turnbull D, Fisher JC. J Chem Phys 1949;17:71.
[42] Price FP. In: Zettlemoyer AC, editor. Nucleation, New York: Marcel Dekker, 1969 (Chap. 8).
[43] Okui N. Polym J 1987;19:1309.
[44] Okui N. J Mater Sci 1990;25:1623.
[45] Janeschitz-Kriegl H, Ratajski E, Wippel H. Colloid Polym Sci 1999;277:217.
[46] Liu T, Mo Z, Wang S, Zhang H. Eur Polym J 1997;33:1405.
[47] Liu S, Yu Y, Cui Y, Zhang H, Mo Z. J Appl Polym Sci 1998;70:2371.
[48] Liu T, Mo Z, Zhang H. J Polym Engng 1998;18:283.
[49] Lee SW, Cakmak M. J Macromol Sci — Phys B 1998;37:501.
[50] Hoffman JD, Weeks JJ. J Res Natl Bur Stand A 1962;66:13.
[51] Alamo RG, Viers BD, Mandelkern L. Macromolecules 1995;28:3205.
[52] Huang J, Prasad A, Marand H. Polymer 1994;35:1896.
[53] Weeks JJ. J Res Natl Bur Stand A 1963;67:441.
[54] Marand H, Xu J, Srinivas S. Macromolecules 1998;31:8219.
[55] Brown RG, Eby RK. J Appl Phys 1964;35:1156.
[56] Lauritzen Jr. JI, Passaglia E. J Res Natl Bur Stand A 1967;71:261.
[57] Schmidtke J, Strobl G, Thurn-Albrecht T. Macromolecules 1997;30:5804.
[58] Hauser G, Schmidtke J, Strobl G. Macromolecules 1998;31:6250.